

Interfacial Charge Transfer between Silver Phosphate and W_2N_3 Induced by Nitrogen Vacancies Enhances Removal of β -Lactam Antibiotics

Yan Lin, Chunping Yang,* Qiuya Niu,* and Shenglian Luo*

Constructing heterojunctions has been demonstrated as an important approach to improve the catalytic performance of photocatalysts, but how to regulate the transfer and separation of photogenerated carriers at the interface is still a great challenge. Herein, W_2N_3 -NV, a two-dimensional transition metal nitride containing nitrogen vacancies, is synthesized by a molten salt-assisted atmosphere calcination method. A novel composite photocatalyst $Ag_3PO_4@W_2N_3$ -NV with good photocatalytic activity and photostability is prepared for the first time and applied to the efficient removal of β -lactam antibiotics. The composite catalyst shows much superior photocatalytic degradation performance of penicillin and amoxicillin, and the apparent rate constant of which is 77.7 and 42.9 times than that of pure Ag_3PO_4 , respectively. Experimental results and density functional theory calculations confirm that the presence of nitrogen vacancies can drive the formation of defects and dangling bonds on the W_2N_3 -NV surface, which make it easy to combine with Ag_3PO_4 and form new chemical bonds at the interface. The W–O chemical bonds formed at the interface provide a fast transfer channel for the interfacial photogenerated charge, resulting in the boosted carriers transfer and separation ability of $Ag_3PO_4@W_2N_3$ -NV composite. This study provides a new strategy for the interface engineering of highly efficient heterogeneous photocatalysts.

1. Introduction

In recent decades, antibiotics have been widely used as one of the most important pharmaceuticals to inactivate or kill pathogen in humans and livestock.^[1,2] It was reported that the annual use of antibiotics was nearly 1.62 million, 13, and 10 thousand tons in China, the USA, and Europe, respectively.^[3] Antibiotics are inevitably released into the environment during their production and use, for example through the pharmaceutical industries, hospital effluents, and the excretions from humans and livestock.^[4,5] The presence of antibiotics in environment, particularly in wastewater and drinking water, even at low concentrations, can lead to the emergence of resistant bacteria problem threatening human health.^[6–9] The β -lactam antibiotics are the most frequently used antibiotics, accounting for more than 50% of the total worldwide antibiotic consumption.^[10] In addition, penicillin G (PNL) and amoxicillin (AMX) are among the most commonly used β -lactam antibiotics, which are also the most vulner-

able to leakage into the environment.^[11] For example, Lu et al. investigated 15 target antibiotics in the water of Jiaozhou Bay in China, and the results indicated that the AMX contamination accounted for 44% of the total concentration of antibiotics, which was the highest proportion among the 14 detected antibiotics.^[12] Given the potential risks posed by antibiotic contamination, it is essential to explore advanced treatments for the degradation or elimination of pharmaceuticals and their metabolites.

Photocatalysis is considered as a green and efficient environmental pollution treatment technology, which can decompose pollutants only by using solar energy.^[13–15] The development of photocatalysts with high photocatalytic performance and stability is the key to this technology.^[16,17] As a classical visible light-responsive semiconductor photocatalyst, silver phosphate (Ag_3PO_4) has attracted much attention due to its high photocatalytic oxidation ability.^[10,18] However, the defects of poor photostability and unsatisfactory electron–hole separation yield limit the wide application of Ag_3PO_4 . Therefore, various attempts have been made to overcome the abovementioned drawbacks,

Y. Lin, C. P. Yang, Q. Y. Niu, S. L. Luo
College of Environmental Science and Engineering
Hunan University, and Key Laboratory of Environmental Biology
and Pollution Control (Hunan University)
Ministry of Education
Changsha, Hunan 410082, China
E-mail: yangc@hnu.edu.cn; niuqiuya@hnu.edu.cn; slou@hnu.edu.cn

C. P. Yang
Guangdong Provincial Key Laboratory of Petrochemical Pollution
Processes and Control
School of Environmental Science and Engineering
Guangdong University of Petrochemical Technology
Maoming, Guangdong 525000, China

S. L. Luo
Key Laboratory of Jiangxi Province for Persistent Pollutants Control
and Resources Recycle
Nanchang Hangkong University
Nanchang, Jiangxi 330063, China

 The ORCID identification number(s) for the author(s) of this article can be found under <https://doi.org/10.1002/adfm.202108814>.

DOI: 10.1002/adfm.202108814

such as morphology optimization,^[19] ion doping,^[20] facet engineering,^[21] and heterojunction construction.^[22,23]

The construction of heterojunction to promote the generation and migration of photogenerated carriers has been proved to be an effective modification method to improve the photocatalytic performance of Ag_3PO_4 . However, it remains challenges in selecting appropriate additives and efficient interfacial charge transfer. Recently, 2D materials have attracted much attention because of their superior properties.^[24] For example, the 2D layered materials can provide more active reaction sites and rich surface area for solar energy harvesting. In addition, the atomic thickness can minimize the carrier's migration distance from the interior to the surface, thus reducing carrier recombination and improving catalytic performance. Moreover, the large specific surface area makes it easy for 2D materials to combine with other materials to construct multicomponent composite catalysts.

Notably, 2D transition metal nitrides (TMNs) which combine the advantages of 2D materials and metal nitrides, have emerged as promising materials in the field of energy storage and catalysis.^[25] For example, Jin et al. synthesized nitrogen-rich 2D TMN material, Mo_5N_6 , which displayed outstanding activity for the hydrogen evolution reaction.^[26] Yu et al. also reported that nitrogen-rich tungsten nitrides such as W_2N_3 and W_3N_4 were decent candidates for catalytic reactions because the electrical structure of W atoms can be tuned by nitrogen atoms.^[27] In view of the above successful cases and the excellent characteristics of W_2N_3 , it should be feasible to utilize W_2N_3 as an additive to improve the photocatalytic performance of Ag_3PO_4 .

Maximizing interfacial charge transfer is another important bottleneck that needs to be solved. It was reported that vacancies, as a typical atomic defects or imperfections, have been demonstrated to effectively modulate the physicochemical, electronic, and catalytic properties of materials.^[28] Chen et al. found that the formation of Sn vacancies could promote the exposure of active CoFe sites, modulated the conductivity, and thus enhanced the performance of oxygen evolution reaction.^[29] Li et al. reported that the co-existence of surface and bulk oxygen vacancies in TiO_2 exhibited a synergistic effect to improve the photoreduction efficiency of CO_2 to CH_4 .^[30] It was found that nitrogen vacancies on W_2N_3 can provide an electron-deficient environment which not only facilitates nitrogen adsorption, but also lowers the thermodynamic limiting potential of nitrogen reduction reaction.^[31] The above reports demonstrated that the introduction of nitrogen vacancies can regulate the electronic structure of material and form new binding sites, which are expected to open up channels at interface to further promote electron transfer.

However, to the best of our knowledge, no information was reported about using 2D W_2N_3 with nitrogen vacancies to prepare Ag_3PO_4 -based heterostructure photocatalysts and construct electron transfer channels at interface. Therefore, in this study, the 2D W_2N_3 was synthesized using molten salt method and the W_2N_3 with nitrogen vacancies ($\text{W}_2\text{N}_3\text{-NV}$) was prepared by annealing W_2N_3 under H_2 atmosphere. The novel $\text{Ag}_3\text{PO}_4@ \text{W}_2\text{N}_3\text{-NV}$ composite was prepared for the first time, and applied to the efficient removal of β -lactam antibiotics. The microstructure, properties, photocatalytic activity, stability, and charge separation mechanisms of as-prepared catalysts were explored

and discussed in detail. The results indicated that the resultant composite photocatalyst exhibited excellent photocatalytic activity on the degradation of PNL and AMX, and the removal rates could reach 100% within 8 and 1 min, respectively. The highly efficient performance was ascribed to the introduction of 2D W_2N_3 and the formation of N vacancies in W_2N_3 , which can benefit the interfacial charge transfer and thus facilitate the photocatalytic degradation performance. These findings open up new possibilities for synthesizing heterogeneous photocatalysts with high photocatalytic performance through interface engineering.

2. Results and Discussion

2.1. Characterization of Materials

The $\text{W}_2\text{N}_3\text{-NV}$ nanosheets were prepared by molten salt-assisted atmosphere calcination method. First, the 2D $\text{Na}_2\text{W}_4\text{O}_{13}$ were synthesized using molten salts method, which was reported as a rapid mass production method.^[32] Then, the nitrogen-rich W_2N_3 nanosheets were prepared by annealing $\text{Na}_2\text{W}_4\text{O}_{13}$ under ammonia atmosphere. Finally, the W_2N_3 with abundant nitrogen vacancies ($\text{W}_2\text{N}_3\text{-NV}$) were produced by annealing 2D W_2N_3 nanosheets under hydrogen atmosphere. The scanning electron microscope (SEM) images of $\text{W}_2\text{N}_3\text{-NV}$ were shown in Figure 1a,b; it could be clearly observed that the $\text{W}_2\text{N}_3\text{-NV}$ presented as a 2D nanosheets morphology. The transmission electron microscope (TEM) images (Figure 1c) showed the 2D morphology of $\text{W}_2\text{N}_3\text{-NV}$ with an average size of 450 nm. Moreover, high-resolution TEM (HRTEM) and selected area electron diffraction (SAED) were carried out to further investigate the orientation and crystal quality of $\text{W}_2\text{N}_3\text{-NV}$. The interplanar spacing of 0.25 nm was clearly observed, which corresponded to the (100) facets of $\text{W}_2\text{N}_3\text{-NV}$ (Figure 1d). The SAED pattern in Figure 1e revealed the single-crystalline hexagonal structure of $\text{W}_2\text{N}_3\text{-NV}$. The atomic force microscopy measurement indicated that the thickness of $\text{W}_2\text{N}_3\text{-NV}$ nanosheet was about 0.82–0.85 nm (Figure 1f,g and Figure S1, Supporting Information).

In order to explore the changes in the structure and properties of the W_2N_3 material after annealing in a hydrogen atmosphere, the X-ray diffraction (XRD) and X-ray photoelectron spectroscopy (XPS) were first carried out. The XRD patterns in Figure 2a indicated that the W_2N_3 and $\text{W}_2\text{N}_3\text{-NV}$ possessed almost the same peak positions, demonstrating the crystal structure of W_2N_3 remained unchanged during hydrogen annealing. The characteristic peaks at 2θ values of 36.3° , 37.1° , 46.2° , 64.8° , and 76.7° could be attributed to the (100), (101), (105), (110), and (106) plane of W_2N_3 respectively, which were in good agreement with the standard pattern.^[33] Moreover, the XPS spectrum in Figure S2, Supporting Information, indicated that the chemical composition of W_2N_3 did not change after annealing in hydrogen atmosphere, which was consistent with the results obtained by XRD. The high-resolution W 4f XPS spectra is shown in Figure 2b and Table S4, Supporting Information; the peaks at 35.29 and 33.12 eV, correspond to the $\text{W}4f_{5/2}$ and $\text{W}4f_{7/2}$ characteristic peaks of W_2N_3 , respectively.^[27] Interestingly, the W4f peaks in $\text{W}_2\text{N}_3\text{-NV}$ were negatively shifted by about 0.2 eV, implying that the valence state of W decreased after H_2 annealing. Besides, the

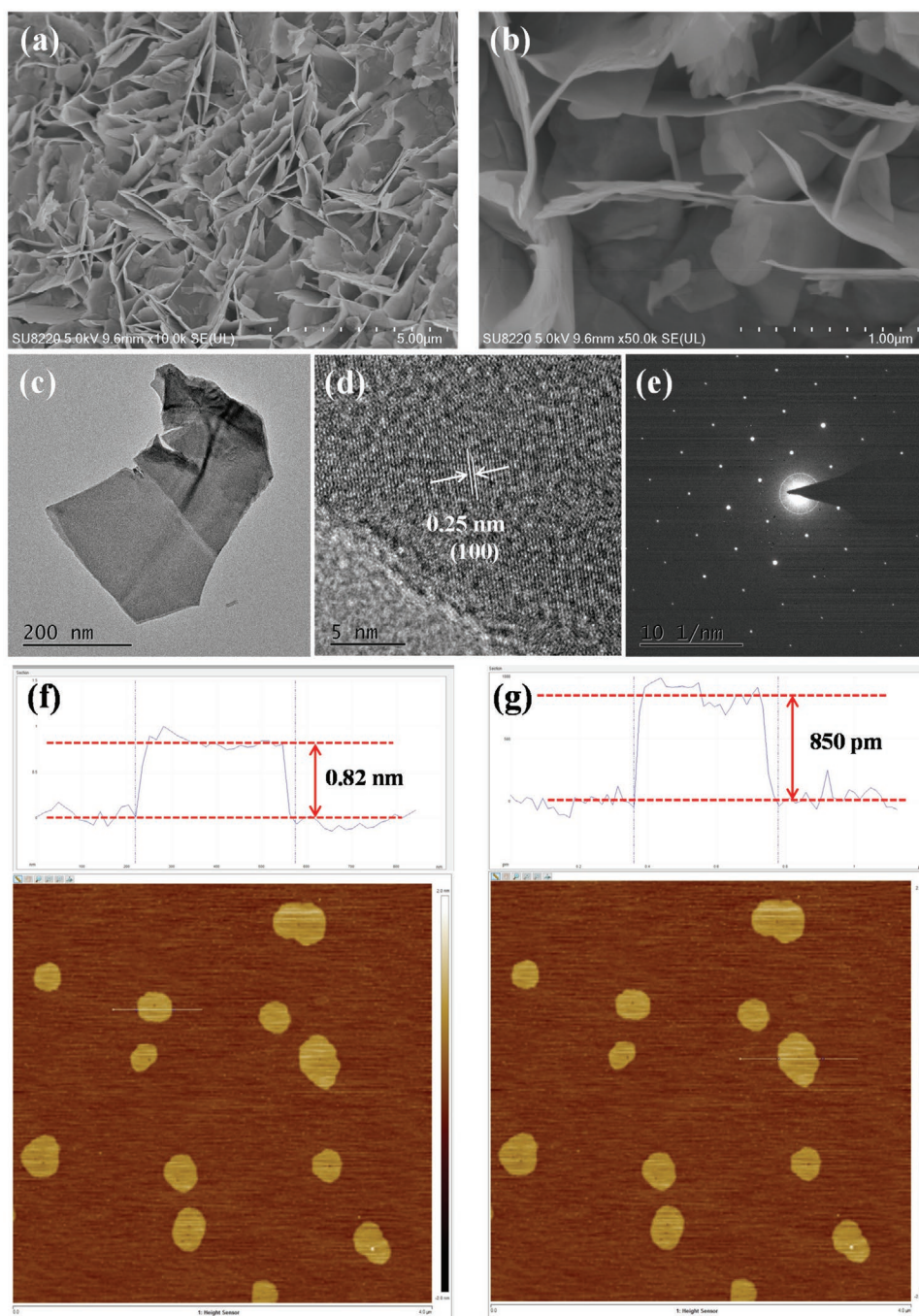


Figure 1. a,b) SEM images, c) TEM image, d) HRTEM image, e) SAED image, and f,g) AFM images of W_2N_3 -NV.

N 1s spectrum in Figure 2c could be deconvoluted into two peaks of 397.7 and 399.5 eV, which corresponded to lattice nitrogen and nitrogen vacancy, respectively. Obviously, the peak intensity of nitrogen vacancy was significantly enhanced after annealing in H_2 . In order to further explore the formation of nitrogen vacancy after annealing under hydrogen atmosphere, the W_2N_3 and W_2N_3 -NV were characterized by electron paramagnetic resonance (EPR) technology, and the results are shown in Figure 2d. The W_2N_3 -NV respond with a characteristic nitrogen vacancy-based EPR feature at $g = 1.9994$, the signal intensity of which

was significantly higher than that of W_2N_3 . The SEM-EDS test of W_2N_3 -NV and W_2N_3 were further carried out to explore the N vacancies, and the results are shown in Figure S5, Supporting Information. The results indicated that the concentration of N vacancies in W_2N_3 and W_2N_3 -NV was about 3.33% and 7.70% respectively (%: percentage of nitrogen atoms removed), which agree well with previous report.^[31]

To investigate the local atomic arrangement and specific bonding modes of W_2N_3 and W_2N_3 -NV, synchrotron radiation X-ray absorption fine structure (XAFS) measurements at the

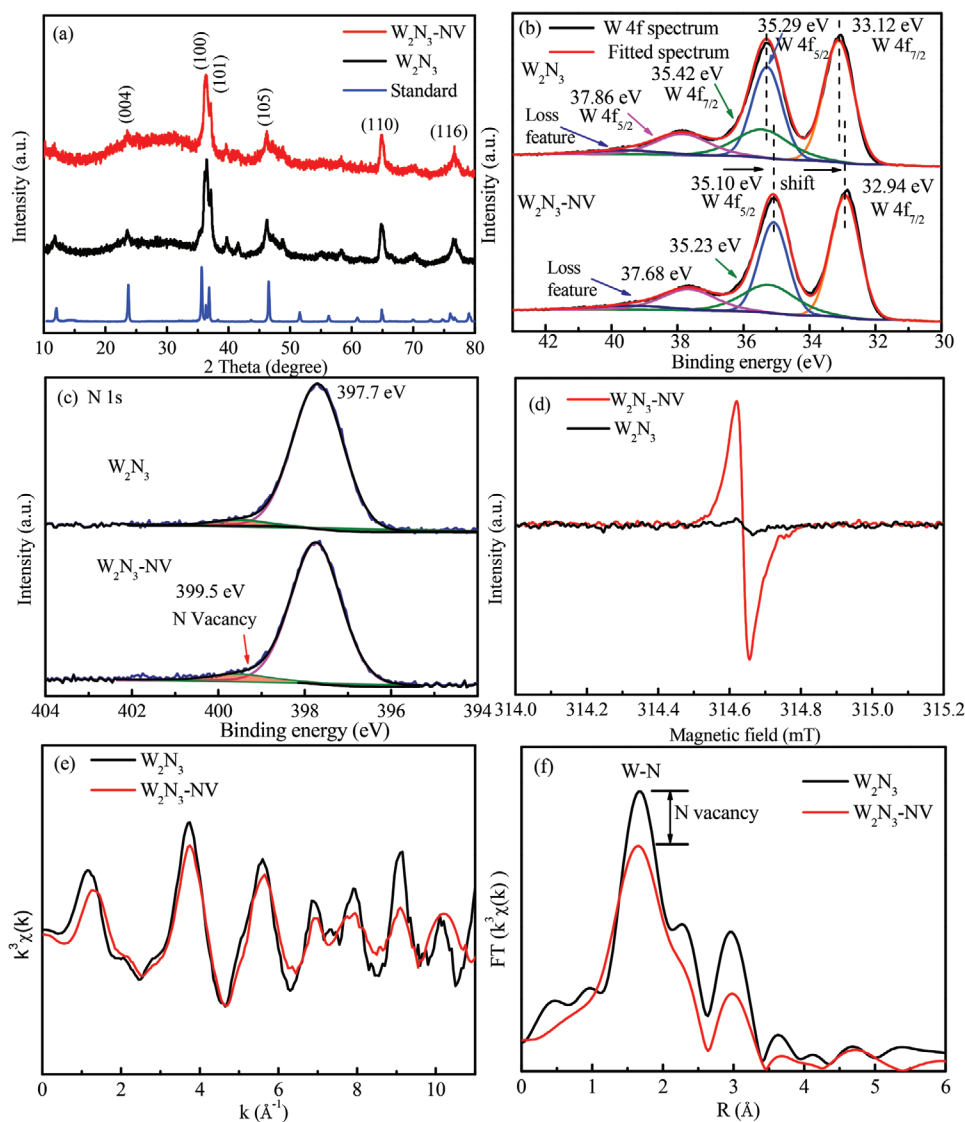


Figure 2. a) XRD pattern, high resolution XPS spectrum of b) W 4f and c) N 1s, d) EPR spectra, e) W L_3 -edge extended XAFS oscillation function $k^3\chi(k)$, and f) Fourier transform (FT) EXAFS spectra of as-prepared W_2N_3 and W_2N_3 -NV.

W L_3 -edge were performed, and the normalized curves were provided in Figure S3a, Supporting Information. As shown in Figure 2e, the W L_3 -edge oscillation curve of W_2N_3 -NV demonstrated a difference in the peak intensity compared to the W_2N_3 , which was attributed to the decreased W–N and W–W coordination.^[27,34] The corresponding Fourier transform extended X-ray absorption fine structure (EXAFS) spectra were also provided in Figure 2f. It could be observed that a main coordination peak at 1.8 Å was assigned to W–N bonding.^[31] The intensity of the characteristic peak for W_2N_3 -NV decreased obviously compared to that of the W_2N_3 , indicating the number of W–N bonds was reduced and the presence of nitrogen vacancies. The quantitative EXAFS analysis is presented in Figure S3, Supporting Information, and the results are summarized in Table S1, Supporting Information. It was found that the coordination number of W–N decreased from 6.0 to 5.75 after hydrogen annealing, which further proved the formation of nitrogen vacancies. In addition, the coordination number of

W–W was also decreased and the disorder degrees increased compared with the W_2N_3 , demonstrating partial dangling bonds and distortion on their surface. The defects and dangling bonds on the surface may make W_2N_3 -NV easy to combine with Ag_3PO_4 , or rebond at the interface, providing channels and media for charge transfer between interfaces.

The SEM images of $Ag_3PO_4@W_2N_3$ -NV are shown in Figure 3a,b, in which the W_2N_3 -NV nanosheets were in close contact with the spherical Ag_3PO_4 , and these spherical crystals grew on the surface of 2D W_2N_3 -NV. The SEM-EDS elemental mapping images of $Ag_3PO_4@W_2N_3$ -NV composites were also performed and the results are shown in Figure 3c–h, which indicated that as-prepared samples consisted of Ag, O, P, W, and N elements. The uniform distribution of W and N implied that W_2N_3 -NV nanosheets were evenly distributed in the $Ag_3PO_4@W_2N_3$ -NV composite. In addition, the TEM image of $Ag_3PO_4@W_2N_3$ -NV is shown in Figure 4a; it could be clearly observed that W_2N_3 -NV nanosheets was in good contact

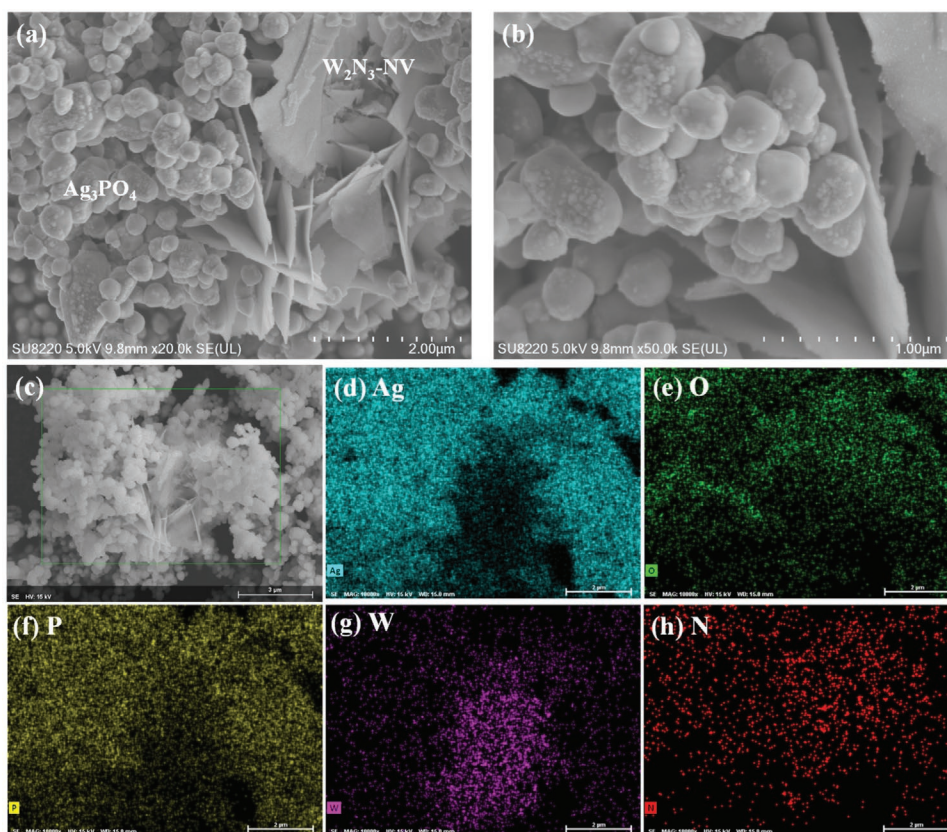


Figure 3. a,b) SEM images and c–h) SEM-EDS elemental mapping images of $\text{Ag}_3\text{PO}_4@W_2N_3\text{-NV}$ composite.

with Ag_3PO_4 . The TEM-EDS elemental mapping images of $\text{Ag}_3\text{PO}_4@W_2N_3\text{-NV}$ composites were also performed and the results are shown in Figure 4d–i, which further demonstrated the consist of Ag, O, P, W, and N elements in the composites and the uniform distribution of elements. The HRTEM image of composite catalyst is presented in Figure 4b; the interplanar spacing of 0.25 nm which corresponded to the (100) facets of $W_2N_3\text{-NV}$ could be clearly observed. Moreover, the SAED pattern in Figure 4c demonstrated that $W_2N_3\text{-NV}$ kept its single-crystalline hexagonal structure in the composite catalyst, indicating there was no structural transformation happening on $W_2N_3\text{-NV}$ after the deposition of Ag_3PO_4 . The results of Figures 3 and 4 both proved the successful synthesis of $\text{Ag}_3\text{PO}_4@W_2N_3\text{-NV}$ composites.

The XRD was used to characterize the prepared Ag_3PO_4 and $\text{Ag}_3\text{PO}_4@W_2N_3\text{-NV}$, as shown in Figure 5a. For pure Ag_3PO_4 , the diffraction peaks coincided with the standard pattern (JCPDS 06-0505). The peaks at 20.88° , 29.69° , 33.29° , and 52.69° could be attributed to the (110), (200), (210), and (222) of Ag_3PO_4 . Compared with the pure Ag_3PO_4 , the diffraction peak position of $\text{Ag}_3\text{PO}_4@W_2N_3\text{-NV}$ has no difference, but the peak intensity of different crystal faces has changed. The peak intensity ratio of (110) to (100) for Ag_3PO_4 was 0.767:1, while that of $\text{Ag}_3\text{PO}_4@W_2N_3\text{-NV}$ composite was 0.808:1. Besides, the peak intensity ratio of (222) to (100) for Ag_3PO_4 was 0.803:1, and that of the composite catalyst was 1.345:1. According to previous reports, different crystal faces have different surface energy, which will directly affect the catalytic activity of the catalysts.^[35]

In order to further investigate the surface energies of Ag_3PO_4 {100}, {110}, and {111} planes, the density functional theory (DFT) calculations were carried out. The different surfaces slab models including 192 atoms were constructed as shown in Figure 6, and the vacuum thickness was set as 20 Å. The surface energy (γ) was calculated using the follow formula:

$$\gamma = \frac{E_{\text{slab}} - NE_{\text{bulk}}}{2A} \quad (1)$$

where E_{slab} is the total energy of the slab and E_{bulk} is the total energy of the bulk per unit cell. N and A are the number of bulk unit cells contained in the slab and the surface area of each side of the slab.^[35,36] The calculation results were summarized in Table 1; the surface energy of {111}, {110}, and {111} facets were 0.522, 0.240, and 0.207 J m⁻², respectively, indicating that the (111) facets possessed the largest surface energy. Moreover, the surface energy of {111} facets was higher than that of {100} facets. Because the crystal faces with higher surface energy have high reactivity, the $\text{Ag}_3\text{PO}_4@W_2N_3\text{-NV}$ composite with more exposed high reactive facets should show higher photocatalytic performance and be conducive to the decomposition of organic molecules.

The chemical compositions of Ag_3PO_4 and $\text{Ag}_3\text{PO}_4@W_2N_3\text{-NV}$ composites were investigated by XPS. The pattern in Figure 5b presented the high-resolution XPS spectrum of Ag 3d. For the composite catalysts, the binding energies at 374.21 and 368.21 eV belong to the Ag 3d_{3/2} and Ag 3d_{5/2}, respectively. Compared with the pure Ag_3PO_4 , the Ag 3d_{3/2} and Ag 3d_{5/2}

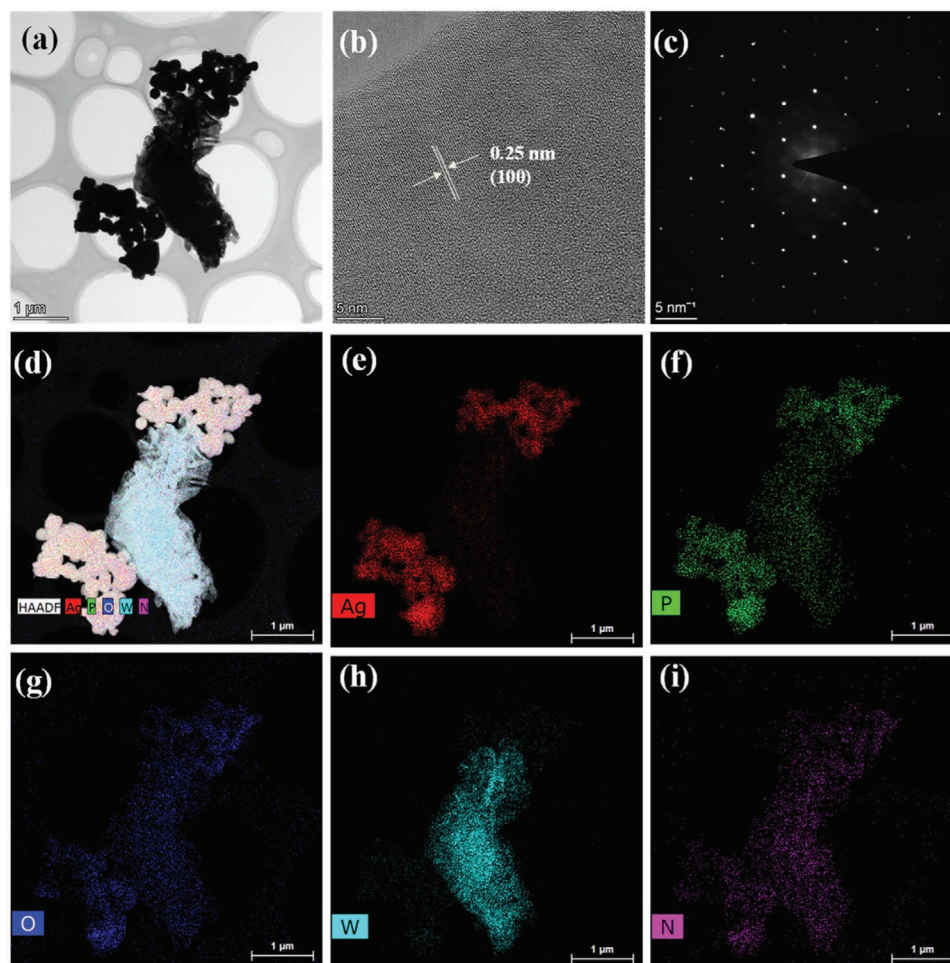


Figure 4. a) TEM image, b) HRTEM image, c) SAED image, and d–i) TEM-EDS elemental mapping images of $\text{Ag}_3\text{PO}_4@W_2N_3\text{-NV}$ composite.

of $\text{Ag}_3\text{PO}_4@W_2N_3\text{-NV}$ composites were shifted to a positive position. Similarly, the high-resolution XPS spectra of P 2p in Figure 5c also indicated that the binding energy of P 2p moved from 133.03 to 133.18 eV after Ag_3PO_4 was combined with the $W_2N_3\text{-NV}$. The O 1s spectrum of Ag_3PO_4 could be deconvoluted into two peaks with binding energies of 530.75 and 531.99 eV, respectively. The peak at 530.75 eV was assigned to the lattice oxygen species, and the peak located at 531.99 eV was attributed to the chemisorbed oxygen species on surface.^[37] Interestingly, after coupling with $W_2N_3\text{-NV}$, the binding energy attributed to the lattice oxygen shifted from 530.75 eV to a negative position of 530.63 eV (Figure 5d). In addition, in the W 4f spectrum of $\text{Ag}_3\text{PO}_4@W_2N_3\text{-NV}$ composites, it could be clearly observed that there was a strong peak that could be deconvoluted into a double peak with binding energy of 36.74 and 38.69 eV, corresponding to the $W 4f_{7/2}$ and $W 4f_{5/2}$ of W–O (WO_3), respectively. Moreover, a signal belonging to W(VI)–O appeared, which also could be deconvoluted into two peaks with binding energies of 38.51 and 40.41 eV, respectively. (Figure 5e and Table S5, Supporting Information).^[38] For pure $W_2N_3\text{-NV}$, the peak at binding energy of 35.23 and 37.68 eV was also assigned to the $W^{6+}4f_{7/2}$ and $W 4f_{5/2}$ of W–O, respectively, which was induced by the ineluctable surface oxidation.^[39] Compared with pure

$W_2N_3\text{-NV}$, the peak intensity of W–N decreased obviously and the signal of W–O was significantly enhanced, which was due to the formation of W–O bonds between the W from $W_2N_3\text{-NV}$ and the O from Ag_3PO_4 . This result was consistent with the analysis results from Figure 2. Nitrogen vacancy presence and the reduction in the number of W–W bonds resulted in the formation of W-hanging bonds on the $W_2N_3\text{-NV}$ surface. As shown in Figure 5f, the N 1s spectrum of $\text{Ag}_3\text{PO}_4@W_2N_3\text{-NV}$ appeared as a main peak with binding energy of 396.6 eV, which was assigned to the dominated N species from $W_2N_3\text{-NV}$.^[40] Compared with the N1s spectrum of $W_2N_3\text{-NV}$, there was a negative shift in composite catalyst, which implied that after the combination of Ag_3PO_4 and $W_2N_3\text{-NV}$, there were electrons transferred from Ag_3PO_4 to $W_2N_3\text{-NV}$. The analysis results of XPS survey indicated that some new W–O bonds were formed at the interface of Ag_3PO_4 and $W_2N_3\text{-NV}$, and there were intensive interaction and intense charge transfer.

The optical properties of as-prepared samples were studied by UV–vis absorption spectroscopy, and the results are shown in Figure 7a. It could be found that the pure Ag_3PO_4 has an absorption edge at about 550 nm, corresponding to a band gap at 2.33 eV (Figure S6, Supporting Information). After coupling with $W_2N_3\text{-NV}$, the composite catalysts showed an obviously

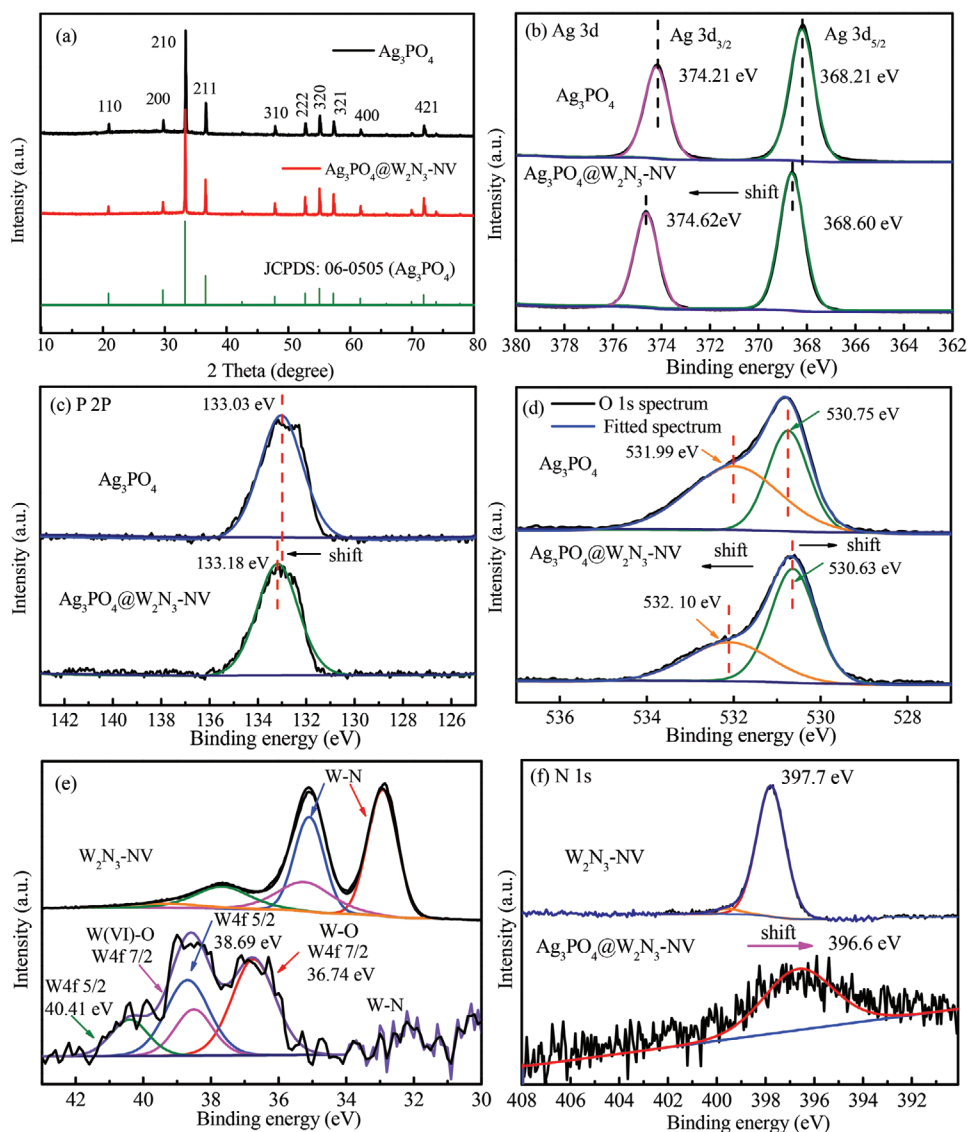


Figure 5. a) XRD pattern of as-prepared samples and high resolution XPS spectrum of b) Ag 3d, c) P 2p, d) O 1s, e) W 4f, and f) N 1s.

enhanced absorption in the whole wavelength range, which was conducive to the improvement of photocatalytic activity. The energy band position was determined by the Mott–Schottky plots and XPS valence band spectra. The Mott–Schottky plot was used to characterize the flat band potential, and the values were determined using the Mott–Schottky equation:

$$\frac{1}{C_{sc}^2} = \frac{2}{\epsilon\epsilon_0 N} \left(E - E_{fb} - \frac{KT}{e} \right) \quad (2)$$

where C_{sc} is the capacitance of the space charge region, ϵ , ϵ_0 , and N are the dielectric constant of semiconductor, the permittivity of free space, and the donor density, respectively.^[41,42] Where E , E_{fb} , K , T , and e are the applied potential, flat band potential, Boltzmann's constant, temperature, and electronic charge, respectively. The value of KT/e is calculated as 0.0257, and the applied potential (E) is determined as 0.42 V (Figure 7b). The flat band potential (E_{fb}) thus could be calculated as 0.39 V

versus the saturated calomel electrode, which was equivalent to 0.63 V versus the normal hydrogen electrode. Because the conduction band potential (E_{CB}) of n-type semiconductors is about 0.2 V lower than the E_{fb} , the value of E_{CB} was 0.43 V versus NHE. The band gap of Ag_3PO_4 is 2.33 eV, so its valence band potential (E_{VB}) was calculated as 2.76 V versus NHE. Moreover, the XPS valence band spectra were carried out to further verify the energy band potential, and the results are depicted in Figure S6b,c, Supporting Information. It could be found that the E_{VB} of Ag_3PO_4 was 2.78 eV, which was in good agreement with the results of Mott–Schottky plots. The highly positive VB position of Ag_3PO_4 exhibited its strong oxidation ability, which was in favor of efficient photocatalytic performance. Interestingly, the flat band potential obtained from Mott–Schottky plots and the valence band potential obtained by XPS-VB spectra both indicated there was a slight negative shift in energy band after the Ag_3PO_4 combined with W_2N_3-NV , which also implied that there was a strong interaction between Ag_3PO_4 and W_2N_3-NV .

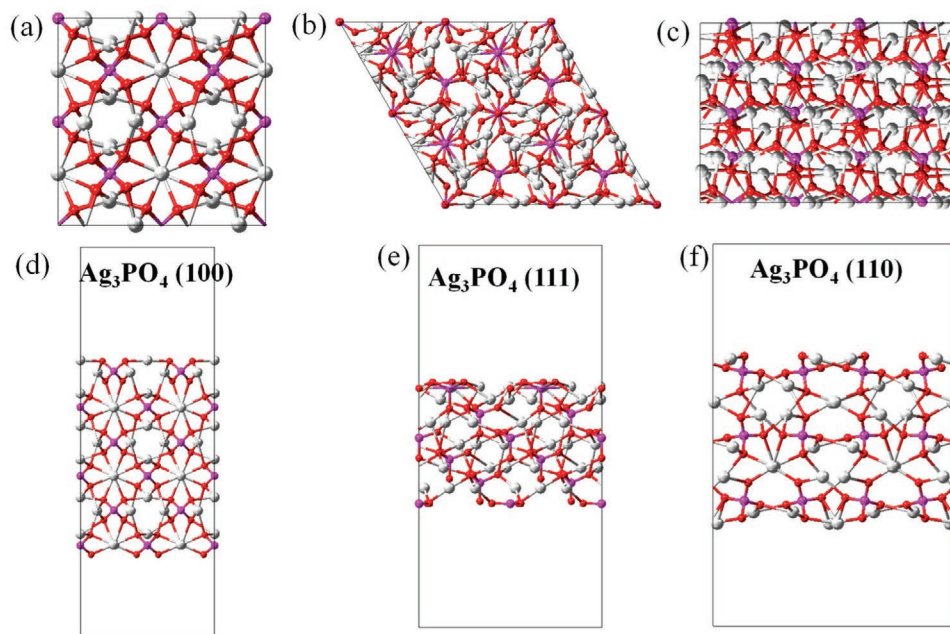


Figure 6. Optimized geometry structures of a,d) $\text{Ag}_3\text{PO}_4(100)$, b,e) $\text{Ag}_3\text{PO}_4(111)$, and c,f) $\text{Ag}_3\text{PO}_4(110)$; (a–c: top view; d–f: side view).

In order to investigate the separation efficiency of photo-generated carriers, the photoluminescence technique was first employed to investigate the recombination of photogenerated electron–hole pairs.^[43] As shown in Figure 7c, the photoluminescence intensity for $\text{Ag}_3\text{PO}_4@W_2N_3\text{-NV}$ was decreased obviously in comparison to that of pure Ag_3PO_4 , demonstrating that the charge separation efficiency was improved significantly after coupling with Ag_3PO_4 and $W_2N_3\text{-NV}$. The time resolution photoluminescence (TRPL) spectrum was also obtained to evaluate the charge separation dynamics processes of as-prepared samples (Figure 7d). The decay curves were fitted with exponentials to obtain the decay time, and the detailed calculation process and data were provided in Supporting Information and Table S2, Supporting Information. The results showed that Ag_3PO_4 have two lifetimes of 1.32 and 6.71 ns. The short decay time component (τ_1) is considered to be caused by the quasi-free excitons,^[44] and the long lifetime component (τ_2) is due to the local exciton recombination caused by the detrapping of carriers.^[45] After combining with $W_2N_3\text{-NV}$, the τ_1 and τ_2 were decreased to 1.19 and 5.48 ns, respectively. The average charge carrier lifetime of Ag_3PO_4 and $\text{Ag}_3\text{PO}_4@W_2N_3\text{-NV}$ was thus calculated as 3.23 and 2.63 ns respectively, indicating a shorter lifetime was obtained after introduction of $W_2N_3\text{-NV}$. The results may be attributed to an additional nonradiative

decay channel opened through the electron transfer between Ag_3PO_4 and $W_2N_3\text{-NV}$, which efficiently facilitated the separation of photogenerated electrons and holes.^[46,47] Moreover, the photocurrent-time response was measured to reflect the photogenerated carrier transportation (Figure 7e). It could be clearly observed that the photocurrent density of $\text{Ag}_3\text{PO}_4@W_2N_3\text{-NV}$ was much higher than that of pure Ag_3PO_4 , which also demonstrated that the photogenerated electrons and holes pairs could be effectively separated after the formation of heterojunction. Electrochemical impedance spectroscopy (EIS) was conducted to further study the photogenerated carrier transfer rate of as-prepared samples. The EIS Nyquist plot consists of one dominant semicircle, and the radius of which is related to the charge-transfer resistance at the interface of sample and electrolyte. The smaller radius arc represents the sample with lower charge-transfer resistance.^[48] As shown in Figure 7f, the EIS Nyquist curve radius of $\text{Ag}_3\text{PO}_4@W_2N_3\text{-NV}$ composite was much smaller than that of Ag_3PO_4 , indicating that the charge separation and transport could be accelerated by the introduction of $W_2N_3\text{-NV}$. All the above results demonstrated that the addition of $W_2N_3\text{-NV}$ can significantly enhance the efficiency of photogenerated carrier transport and separation, which would greatly promote the photocatalytic activity of the catalysts.

Table 1. Supercell parameters and DFT calculation results of different Ag_3PO_4 surfaces.

Ag_3PO_4 surfaces	Supercell parameters			E_{slab} [eV]	E_{bulk} [eV]	Surface energy [J m^{-2}]
	a [Å]	b [Å]	Gamma [°]			
(100)	12.02872	12.02872	90	−999.694537	−41.809788	0.207
(111)	17.01118	17.01118	120	−997.303845		0.522
(110)	12.02872	17.01118	90	−987.090243		0.240

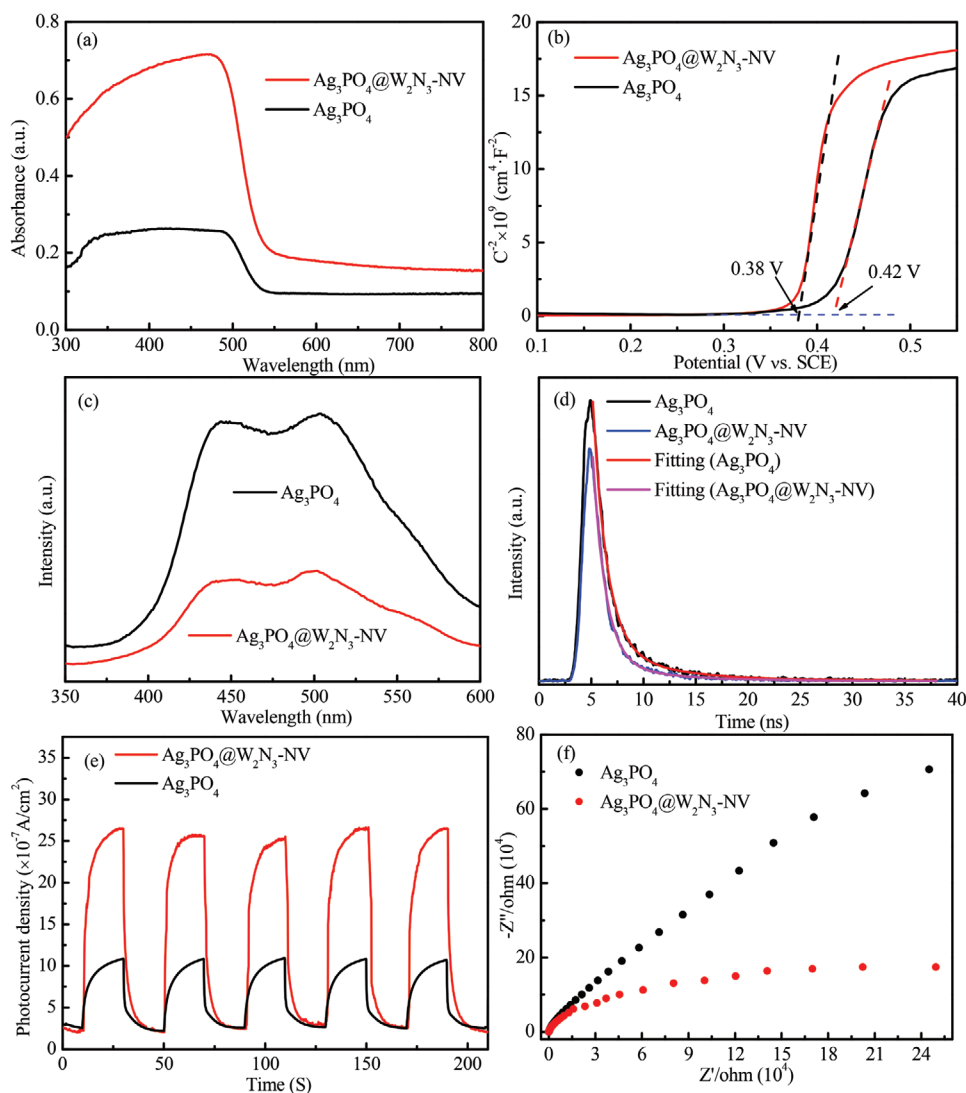


Figure 7. a) UV-vis absorption spectra, b) Mott-Schottky plots, c) PL spectra, d) TRPL decay spectra, e) photocurrent response density, and f) EIS Nyquist plots of as-prepared samples.

2.2. Photodegradation Performance and Photostability of Catalysts

In order to evaluate the photocatalytic activity of as-prepared samples, the experiments in dark and under visible irradiation ($\lambda > 420$ nm) were performed. As shown in **Figure 8a**, the adsorption performance of W_2N_3-NV is very poor, only about 1.0% of AMX was removed. The concentration of AMX also did not further decrease after visible light irradiation, indicating that the pure W_2N_3-NV did not have photocatalytic activity. The photocatalytic activity of pure Ag_3PO_4 was also unsatisfactory. Only 42.5% of AMX was removed after 300 s of illumination, which was due to the high recombination rate of photogenerated carriers and its photocorrosion. Obviously, with the introduction of W_2N_3-NV , all the composite photocatalysts significantly improved its degraded ability for AMX. Especially for $Ag_3PO_4@5$ mL W_2N_3-NV , the degradation rate of AMX reached 94.3% after 40 s of illumination, and reached 100%

after 1 min. The kinetics of the photodegradation of AMX by different samples were fitted with the pseudo-first order reaction model ($-\ln(C/C_0) = kt$), where k is the apparent rate constant. As shown in **Figure S7a**, Supporting Information, it can be seen that the apparent rate constant of $Ag_3PO_4@5$ mL W_2N_3-NV was 0.073 s $^{-1}$, which was 42.9 times higher than that of pure Ag_3PO_4 (0.0017 s $^{-1}$). Moreover, the photocatalytic reaction of Penicillin G (PNL) with different photocatalysts was also carried out, and the results were provided in **Figure 8b** and **Figure S7b**, Supporting Information. Similar results can also be observed, and there was only 12.4% PNL removed after 16 min of irradiation with presence of Ag_3PO_4 , while the degradation efficiency of PNL by $Ag_3PO_4@5$ mL W_2N_3-NV can reach 100% within 8 min of illumination. The apparent rate constant of PNL on the $Ag_3PO_4@5$ mL W_2N_3-NV composite was 0.7 min $^{-1}$, which was 77.7 times than that of the pure Ag_3PO_4 (0.009 min $^{-1}$). The above results indicated that the photocatalytic performance of Ag_3PO_4 was significantly improved after combining with

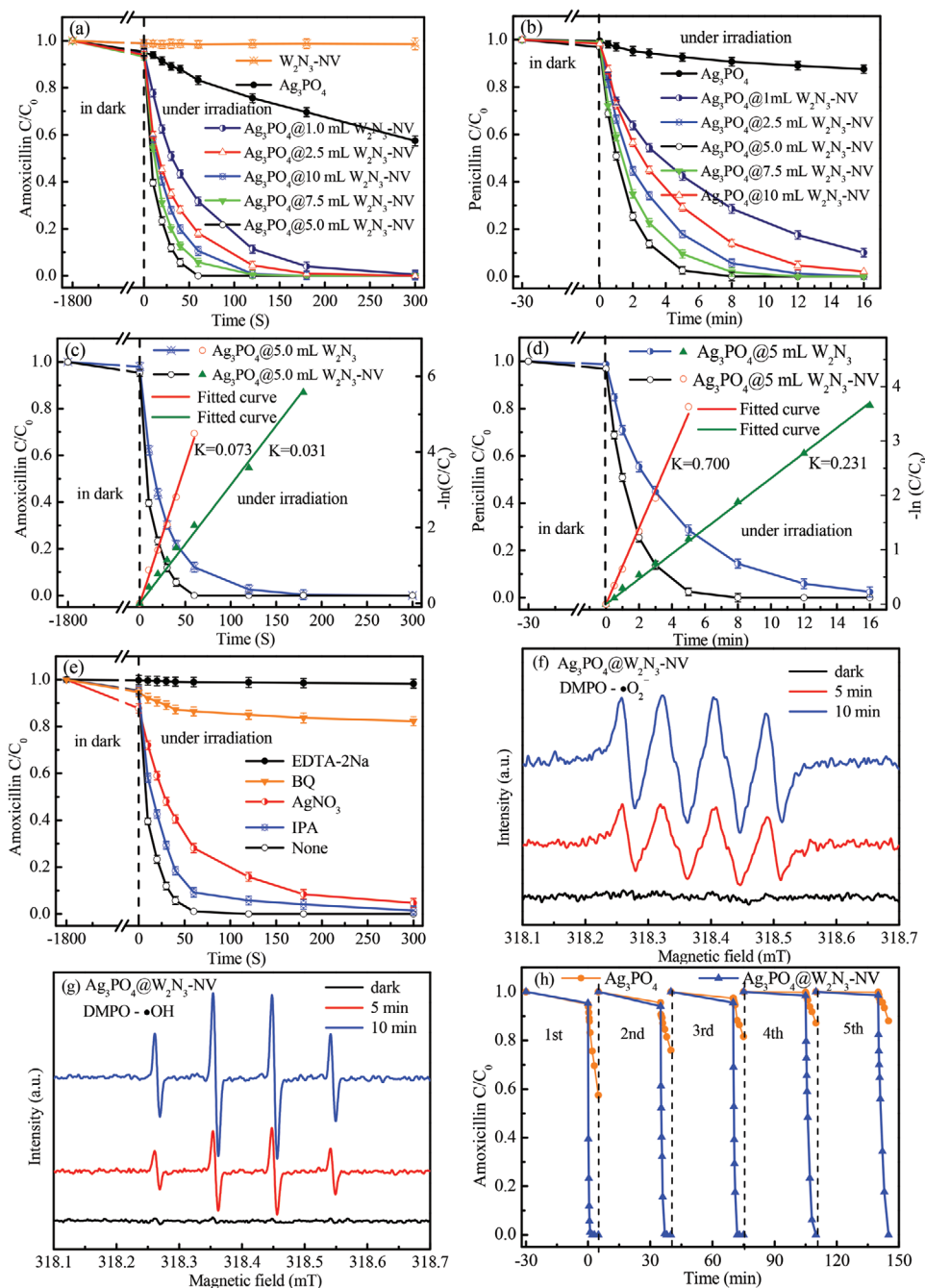


Figure 8. Photocatalytic degradation curves of a,c) AMX and b,d) PNL in the presence of as-prepared samples. e) Photocatalytic degradation curves of AMX over $\text{Ag}_3\text{PO}_4@W_2N_3\text{-NV}$ composite with different active species scavengers. ESR spectra of f) $\text{DMPO}\cdot\text{O}_2^-$ and g) $\text{DMPO}\cdot\text{OH}$ under both the dark and visible light irradiation ($\lambda > 420\text{ nm}$) condition. h) Cycling test for the photocatalytic degradation of AMX in the presence of different samples.

$W_2N_3\text{-NV}$, which was due to the good charge transfer between the interfaces and the efficient photogenerated carrier separation of composite catalysts.

To investigate the effect of nitrogen vacancies on the photocatalytic activity of composite photocatalysts, the optimal composite catalyst $\text{Ag}_3\text{PO}_4@5\text{ mL } W_2N_3\text{-NV}$ was selected as the comparison, thus the $\text{Ag}_3\text{PO}_4@5\text{ mL } W_2N_3$ composite was also prepared using W_2N_3 without annealing in hydrogen atmosphere. According to the analysis results of Figure 2, it

can be seen that W_2N_3 contained almost no nitrogen vacancies. The photocatalytic degradation experiment of AMX and PNL by $\text{Ag}_3\text{PO}_4@5\text{ mL } W_2N_3$ was carried out, and the results as presented in Figure 8c,d. It could be observed that the photocatalytic activity of $\text{Ag}_3\text{PO}_4@5\text{ mL } W_2N_3$ composite was lower than that of $\text{Ag}_3\text{PO}_4@5\text{ mL } W_2N_3\text{-NV}$, and the obtained degradation data were fitted well with the pseudo-first order reaction model. The apparent rate constant of AMX and PNL degradation by $\text{Ag}_3\text{PO}_4@5\text{ mL } W_2N_3\text{-NV}$ was 0.073 s^{-1} and

0.700 min⁻¹ respectively, which was 2.35 and 2.03 times that of Ag₃PO₄@5 mL W₂N₃ (0.031 s⁻¹ and 0.231 min⁻¹), respectively. The results demonstrated that the introduction of nitrogen vacancies on W₂N₃ could further improve the photocatalytic performance of binary composite catalysts, which may result from there being more dangling bonds formed on the surface of W₂N₃-NV. The appearance of nitrogen vacancy promoted the formation of new chemical bonds and charge transfer at the interface between Ag₃PO₄ and W₂N₃-NV, which can significantly facilitate the separation of photogenerated carriers.

In order to explore the active species that played a major role in the photocatalytic reaction of Ag₃PO₄@W₂N₃-NV composite, quenchers of different active species were added to the reaction system.^[49,50] EDTA-2Na, benzoquinone, AgNO₃, and isopropanol (IPA) were used as quenchers for photogenerated holes (h⁺), superoxide radicals (·O₂⁻), photogenerated electrons, and hydroxyl radicals (·OH), respectively. The photocatalytic degradation curves with different quencher presence were shown in Figure 8e. It can be clearly observed that the composite catalyst was almost inactivated in the presence of EDTA-2Na, indicating that photogenerated holes play an important role in the photocatalytic degradation process. In addition, after adding benzoquinone, the removal rate of AMX was only 17.7% after irradiation for 5 min, implying that superoxide radical was another important active species. With the addition of AgNO₃ and IPA, the photocatalytic activity of Ag₃PO₄@W₂N₃-NV composite was also reduced, but the effect was much less than that of EDTA-2Na and benzoquinone. Therefore, the results showed that all the above species contributed to the photocatalytic degradation reaction, while the dominant roles were photogenerated holes and superoxide radicals. To further verify the ability of the composite photocatalyst to produce free radicals, ESR spectra were measured, and the results were shown in Figure 8f,g. It was found that the signal peaks of ·OH and ·O₂⁻ could not be detected in the reaction system under dark condition. After visible light irradiation, high-intensity characteristic peak signals appeared, and the intensity increased with the extension of the illumination time. Due to the positive valence band position of Ag₃PO₄, the photogenerated holes it generated can directly oxidize pollutant molecules, or react with H₂O and OH⁻ to generate ·OH. In addition, the photogenerated electrons readily reacted with oxygen adsorbed on the catalyst surface to form ·O₂⁻. The produced photogenerated holes, ·OH and ·O₂⁻ can all attack the pollutant molecules, and achieve the purpose of degrading and removing pollutants.

The stability of photocatalysts is another important index to evaluate the performance of catalysts, so the recycling degradation experiment of as-prepared Ag₃PO₄ and Ag₃PO₄@W₂N₃-NV has been carried out. In brief, the used photocatalysts were collected after filtration, washing, and drying, and then applied to another round of AMX degradation experiment under the identical conditions. As shown in Figure 8h, after the composite catalyst was recycled for five times, the removal rate of AMX can still reach 100% within 5 min. However, the removal efficiency of AMX by the pure Ag₃PO₄ was decreased from 42.5% to 11.9%, and the reduction rate reached 72%. Such poor stability was due to the serious photocorrosion of pure Ag₃PO₄; its photogenerated electrons easily reacted with the lattice silver to form Ag⁰, thus destroying the crystal structure and

inhibiting the photocatalytic activity. However, after combining with W₂N₃-NV, not only the photocatalytic activity was significantly improved, but also the stability of the composite catalyst was greatly improved. Moreover, the used photocatalysts were characterized by XRD, and the results were provided in Figure S8, Supporting Information. It could be clearly observed that a strong peak at 38.12° appeared in the spectra of used pure Ag₃PO₄, which belongs to Ag (111), indicating that the lattice silver in pure Ag₃PO₄ was indeed reduced to metallic silver by the photogenerated electrons. However, only one weak peak was found in the spectrum of the used Ag₃PO₄@W₂N₃-NV composite catalyst, demonstrating that the composite photocatalyst has good stability and antiphotocorrosion ability. This can be attributed to the abundant electron transfer between Ag₃PO₄ and W₂N₃-NV, resulting in the formation of interfacial charge polarization, and then the built-in electric field was constructed, which promoted the efficient separation of photogenerated carriers.

2.3. Electron Transfer Mechanisms Analysis Using Density Functional Theory Calculations

The above results indicated that the introduction of W₂N₃-NV can effectively promote the photocatalytic activity and stability of the Ag₃PO₄ catalyst, and the XPS results showed that there was a strong interface interaction and electron transfer between Ag₃PO₄ and W₂N₃-NV. Therefore, in order to further explore the electron transfer mechanism, DFT calculations were carried out and the optimized configurations were presented in Figure S9, Supporting Information. First, the work function of W₂N₃-NV and Ag₃PO₄ was calculated, and the results are shown in Figure 9a,b. The work function defined as the potential difference between vacuum and Fermi level, is described in Equation (3):

$$\Phi = E_{\text{vac}} - E_{\text{F}} \quad (3)$$

where Φ is the work function, E_{vac} is the electrostatic potential in a vacuum region, and E_{F} is the Fermi energy.^[51] According to the calculated results, it could be found that the work functions of W₂N₃-NV and Ag₃PO₄(100) were 6.894 and 4.344 eV, respectively, indicating that Ag₃PO₄(100) has higher Fermi level (Figure 10a). When they form a close contact, in order to balance the Fermi energy in the whole composite, the electrons of Ag₃PO₄ will be transferred to W₂N₃-NV. When the Fermi energy is equal to $E_{\text{F}0}$, the energy band near the surface of Ag₃PO₄ will form a potential barrier to prevent the transfer of electrons from W₂N₃-NV to Ag₃PO₄ (Figure 10b). When the composite catalyst was exposed to visible light, the Fermi level of Ag₃PO₄ increased to $E_{\text{F}1}$ to form a quasi-static equilibrium with the energy input and electron transition (Figure 10c). In order to keep the unity of the Fermi level in the whole composite catalysts, a net electron transfer from the CB of Ag₃PO₄ to the W₂N₃-NV will continuously occur, which could effectively promote the separation of photogenerated electrons and holes.

Moreover, the planar averaged self-consistent electrostatic potential for Ag₃PO₄(100)@W₂N₃-NV composite as a function of position in the z-direction was calculated and the results as

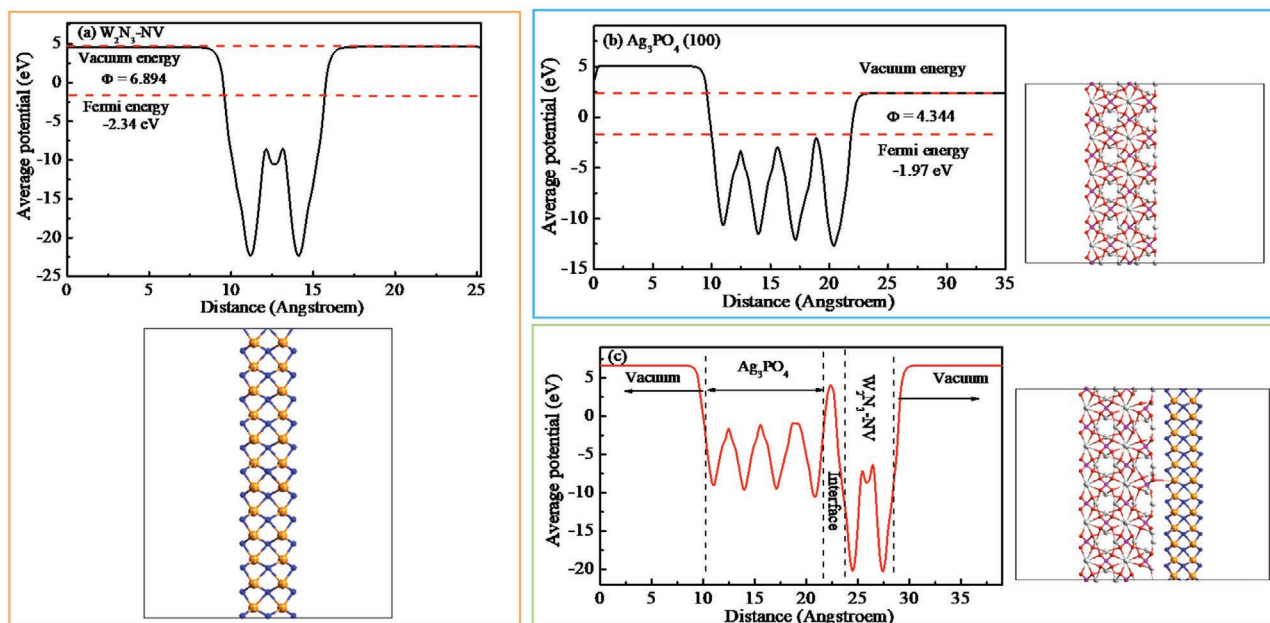


Figure 9. The planar averaged electrostatic potential and work function analysis of a) W_2N_3-NV , b) Ag_3PO_4 , and c) $Ag_3PO_4@W_2N_3-NV$ composite.

shown in Figure 9c. It could be observed that after geometry optimizations, the atoms in the top two layers of $Ag_3PO_4(100)$ were rearranged. The O atom of $Ag_3PO_4(100)$ directly below the defect of N atom in W_2N_3-NV moved up obviously, and a new chemical bond was formed between W and O. The chemical bond formed could provide a new channel for electron transfer between interfaces. As depicted in Figure 9c, although the atoms in the upper layer of $Ag_3PO_4(100)$ moved, the overall periodic lattice potential in the $Ag_3PO_4(100)$ lattice could also be clearly observed. Remarkably, a huge potential well appeared at the interfaces of $Ag_3PO_4(100)$ and W_2N_3-NV , which could significantly promote the electrons transfer between interfaces.

In order to further explore the charge transfer and separation at the $Ag_3PO_4@W_2N_3-NV$ composite, the charge density difference of composite heterostructure was calculated, and the results are depicted in Figure 11a,b. The charge density difference was calculated by Equation (4):

$$\Delta\rho = \rho_{[Ag_3PO_4(100)@W_2N_3-NV]} - \rho_{[Ag_3PO_4(100)]} - \rho_{(W_2N_3-NV)} \quad (4)$$

where $\rho_{[Ag_3PO_4@W_2N_3-NV]}$, $\rho_{[Ag_3PO_4(100)]}$, and $\rho_{(W_2N_3-NV)}$ are the charge densities of the composite, $Ag_3PO_4(100)$ surface, and W_2N_3-NV in the same configuration, respectively.^[23,52] As shown in Figure 11a, the yellow region represented charge depletion, and the green region indicated charge accumulation. It could be clearly observed that the charge redistribution mainly occurred at the $Ag_3PO_4@W_2N_3-NV$ composite interface region, the charge depletion was mainly in the upper region of $Ag_3PO_4(100)$, and charge accumulation was mainly in the lower area of W_2N_3-NV . In addition, the planar-averaged charge density difference along the z-direction was also calculated to reveal the change of charge density, and the results are illustrated in Figure 11b. Positive and negative values represent the accumulation and consumption of charge, respectively. Therefore, the change at interfaces indicated that the electrons transferred

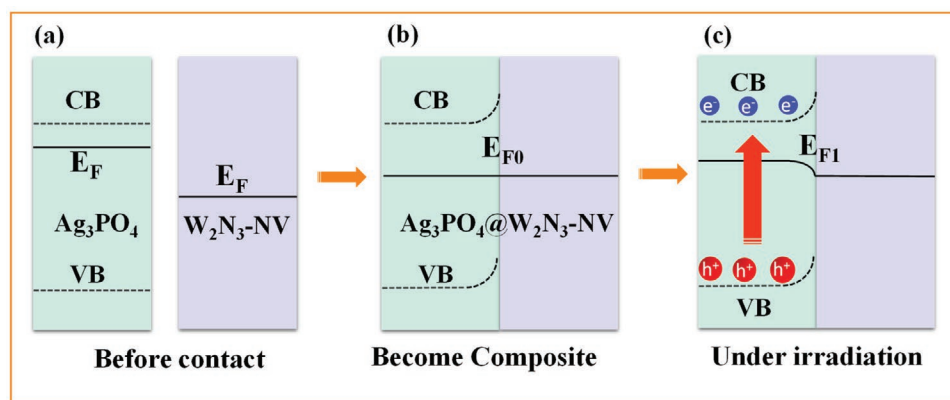


Figure 10. Schematic illustration for the band energetics of Ag_3PO_4 and W_2N_3-NV system: a) before contact, b) become $Ag_3PO_4@W_2N_3-NV$ composite but in the dark, and c) composite catalysts under irradiation.

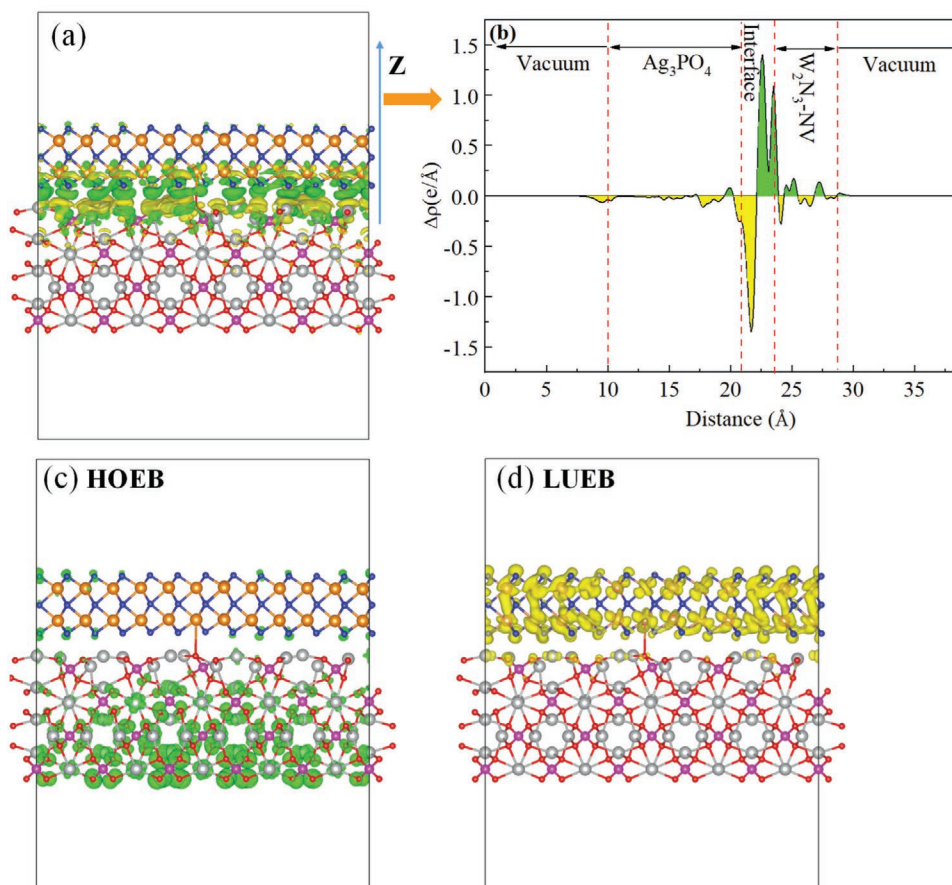


Figure 11. a) 3D charge density difference ($0.001 \text{ e bohr}^{-3}$) for the $\text{Ag}_3\text{PO}_4@W_2N_3\text{-NV}$ composite (green and yellow areas indicate charge accumulation and depletion, respectively). b) Planar-averaged electron density difference $\Delta\rho(z)$ for the composite. The energy band charge density distributions ($0.0003 \text{ e bohr}^{-3}$) of c) the highest occupied energy band (HOEB) and d) the lowest unoccupied energy band (LUEB). The green and yellow colors represent the charge density distribution with and without electron occupation.

from the $\text{Ag}_3\text{PO}_4(100)$ side to the $W_2N_3\text{-NV}$ side across the interface and the chemical bonds, which was good in agreement with the results from the analysis of work functions.

In order to quantify the change of charge density, the Bader charge analysis was also utilized to study the change of charge densities in the $\text{Ag}_3\text{PO}_4@W_2N_3\text{-NV}$ composite heterostructure, and the results are summarized in Table S3, Supporting Information. The results indicated that there was about 2.45 electron transfer from the Ag_3PO_4 layer to the $W_2N_3\text{-NV}$ layer. In addition, the $\text{Ag}_3\text{PO}_4@W_2N_3$ composite heterostructure without N vacancy was constructed, and the same calculation was carried out. The results showed that there was only 2.01 electron transfer at the interface between the Ag_3PO_4 and W_2N_3 , indicating that the appearance of N vacancy can significantly promote the electron transfer at the interface. This was mainly due to the formation of N vacancy, which led to the appearance of W-hanging bond on the surface of $W_2N_3\text{-NV}$. The hanging bond tends to form chemical bond with the O atom of Ag_3PO_4 at the interface, thus forming a new electron transfer channel to promote electron migration.

To investigate the migration direction of photogenerated electrons, the band decomposed charge densities of highest occupied energy band (HOEB) and lowest unoccupied energy

band for the $\text{Ag}_3\text{PO}_4@W_2N_3\text{-NV}$ heterostructure are calculated and shown in Figure 11c,d. It could be clearly observed that the HOEB of the composite heterostructure was occupied by the electron orbitals of Ag_3PO_4 , whereas the HOEB was occupied by the electron orbitals of $W_2N_3\text{-NV}$. Therefore, after the composite photocatalyst was exposed to the visible light, the electrons on Ag_3PO_4 undergo a transition and migrate to $W_2N_3\text{-NV}$, which was in agreement with the analysis results from Figures 9 and 10. Meanwhile, the photogenerated holes remain in the valence band of Ag_3PO_4 , which can directly attack and oxidize organic pollutants.

2.4. Photocatalytic Degradation Mechanism of Photocatalysts

Based on the analysis of the above experimental and calculated results, a reasonable photocatalytic mechanism promoting degradation of β -lactam antibiotics by $\text{Ag}_3\text{PO}_4@W_2N_3\text{-NV}$ composite was proposed, as shown in the Figure 12. Under the visible light irradiation, the Ag_3PO_4 can be easily excited to produce photogenerated electrons (e^-) and holes (h^+). Because of the formation of heterogeneous structure and good interface contact between Ag_3PO_4 and $W_2N_3\text{-NV}$, especially due to the

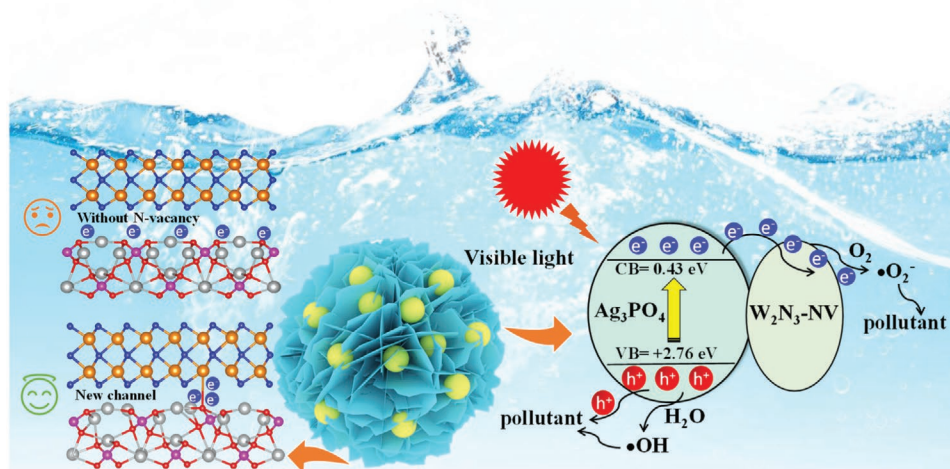


Figure 12. Schematic illustration of photocatalytic degradation mechanism for $\text{Ag}_3\text{PO}_4@W_2N_3\text{-NV}$ composite under visible light irradiation.

presence of N vacancies, the defects and W-hanging bonds were formed on the surface of $W_2N_3\text{-NV}$ catalyst, resulting in the formation of new chemical bonds at the interface. The new chemical bonds can be used as a good electron transfer channel, making it easy to transfer electrons between interfaces. Moreover, the built-in electric potential well at the interface of composite made the $W_2N_3\text{-NV}$ act as an electron sink, which steers the unidirectional electron flow to be trapped by the $W_2N_3\text{-NV}$, thus significantly promoting the separation of photogenerated carriers.

Therefore, the photogenerated electrons produced by Ag_3PO_4 tend to migrate to the $W_2N_3\text{-NV}$, and reacted with the O_2 adsorbed on the surface of the catalysts to generate superoxide radicals ($\cdot O_2^-$). The antibiotic molecules would be attacked by $\cdot O_2^-$, which would be gradually broken down into small molecules and eventually mineralized into water and carbon dioxide. Meanwhile, due to the positive valence band position of Ag_3PO_4 , the photogenerated holes left on the valence band have strong oxidation ability, and they can also directly oxidize pollutant molecules. In addition, it can react with H_2O to produce hydroxyl radicals ($\cdot OH$), which also have the ability to attack and decompose pollutants. Finally, due to the high photocatalytic activity of the composite catalysts and the formation of active species, the antibiotic molecules were rapidly decomposed.

3. Conclusions

In this study, the $W_2N_3\text{-NV}$ was successfully synthesized by annealing 2D W_2N_3 nanosheets under hydrogen atmosphere. As-prepared novel composite photocatalysts $\text{Ag}_3\text{PO}_4@W_2N_3\text{-NV}$ exhibited excellent photocatalytic removal performance for β -lactam antibiotics. After 8 and 1 min of visible light irradiation, the degradation efficiency of PNL and AMX reached 100%, and the reaction rate increased to 77.7 and 42.9 times, respectively. The results of radical trapping experiments and ESR spectra indicated that the active species which play a dominant role in the catalytic degradation process were photogenerated

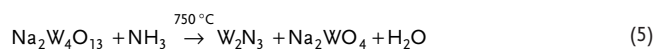
holes and superoxide radicals. The results of DFT calculations, including the work function, Bader charge analysis, 3D charge difference density, and planar averaged self-consistent electrostatic potential, showed that there was a large amount of charge transfer between the interface of Ag_3PO_4 and $W_2N_3\text{-NV}$. The presence of nitrogen vacancies leads to the formation of new chemical bonds at the interface of composite catalysts, which can be used as a channel for rapid charge transfer. The existence of a huge built-in potential well and the difference of Fermi energy levels let $W_2N_3\text{-NV}$ be used as an electron trap to rapidly migrate the photogenerated electrons produced by Ag_3PO_4 to the catalyst surface, so as to significantly promote the efficient separation of carriers and the improvement of catalytic activity. This study developed a novel highly efficient heterojunction photocatalyst that can effectively remove β -lactam antibiotics, and provided a new strategy for interface engineering design of heterojunction catalyst.

4. Experimental Section

Chemicals: Sodium nitrate (NaNO_3), ammonium tungstate ($(\text{NH}_4)_{10}W_{12}O_{41} \cdot xH_2O$), silver nitrate (AgNO_3), ethanol ($\text{CH}_3\text{CH}_2\text{OH}$), disodium hydrogen phosphate dodecahydrate ($\text{Na}_2HPO_4 \cdot 12H_2O$) were obtained from Sinopharm Chemical Reagent Co. Ltd., China, and used without further purification. AMX and Penicillin G (PNL) were purchased from Sigma-Aldrich and used directly.

Synthesis of $\text{Na}_2W_4O_{13}$ Nanosheets: The $\text{Na}_2W_4O_{13}$ nanosheets were prepared by a modified molten-salt method.^[31] In a typical process, 8.0 g of NaNO_3 was added to the crucible and then put into a preheated muffle furnace (350 °C) for 30 min. Next, 0.2 g $(\text{NH}_4)_{10}W_{12}O_{41} \cdot xH_2O$ was added into the above NaNO_3 that had turned to a molten state, and reacted for 60 s. Then, the products were removed from the muffle furnace and naturally cooled to room temperature. Finally, the obtained powder was washed with deionized water for several times to remove extra NaNO_3 , and then freeze-dried to obtain $\text{Na}_2W_4O_{13}$ nanosheets.

Synthesis of W_2N_3 : The W_2N_3 was prepared according to the follow reaction.



First, 0.1 g of $\text{Na}_2W_4O_{13}$ was added into a quartz boat and transferred to the tube furnace, which was calcined at 750 °C for 5 h under 5% NH_3/Ar

atmosphere (heating rate: 5 °C min⁻¹). After cooling down to room temperature naturally, the mixture was washed with deionized water and sonication for 10 min to remove the Na₂WO₄, and the W₂N₃ was collected by centrifugation and freeze-dried for 2 days.

Synthesis of W₂N₃ with Nitrogen Vacancies: The W₂N₃-NV was prepared by annealing W₂N₃ under H₂ atmosphere. In detail, the above W₂N₃ was annealed in 5% H₂/Ar flow at 500 °C for 3 h with a heating rate of 3 °C min⁻¹. After cooling down to room temperature naturally, the W₂N₃-NV was prepared successfully.

Synthesis Ag₃PO₄ and Ag₃PO₄@W₂N₃-NV: The synthetic method of pure Ag₃PO₄ and Ag₃PO₄@W₂N₃-NV was referred from the authors' previously reported method.^[53] First, 0.1 g of as-prepared W₂N₃-NV was added into 200 mL deionized water, and ultrasonically dispersed for 1 h to obtain a W₂N₃-NV suspension. Afterward, 5 mL of W₂N₃-NV suspension was diluted to 30 mL with deionized water, and the AgNO₃ aqueous solution (20 mL, 9 mmol) was added to the above 30 mL of W₂N₃-NV aqueous suspension and then stirred violently in dark for 12 h. Then, the Na₂HPO₄·12H₂O aqueous solution (20 mL, 3 mmol) was added to the above mixture at a rate of 0.1 mL min⁻¹. After maintaining stirring for 6 h in dark condition, the Ag₃PO₄@5 mL W₂N₃-NV was collected by centrifugation, washed by deionized water, and finally dried overnight in vacuum (60 °C). The Ag₃PO₄@W₂N₃-NV composites with different content of W₂N₃ were prepared by changing the volumes of W₂N₃-NV suspension, and the pure Ag₃PO₄ was prepared without adding of W₂N₃-NV.

Computational Details and Methods: All DFT calculations were performed using MedeA-VASP. The calculations were based on DFT and the exchange-correlation potential was described with the GGA-PBE. The Ag₃PO₄(100), Ag₃PO₄(110), and Ag₃PO₄(111) surface models were constructed is shown in Figure 5, which all contain 192 atoms. The electronic iterations convergence was 1.00 × 10⁻⁵ eV using the normal (blocked Davidson) algorithm and real space projection operators. A default planewave cutoff energy of 400.000 eV was used. Since the Ag₃PO₄(100) was the most stable one among the low index surfaces,^[54] a supercell of Ag₃PO₄(100)@W₂N₃-NV was constructed, which included the Ag₃PO₄(100) surface slab and W₂N₃-NV slab. A vacuum layer with a thickness of 20 Å was set to avoid artificial interaction in the supercell (30.27 × 5.83 × 39.10 Å³). Van der Waals interactions were added by means of a forcefield (DFT+D3 approach of S. Grimme with zero-damping).^[55,56] The requested k-spacing was 0.5 per Angstrom, which corresponded to actual k-spacings of 0.208 × 0.359 × 0.161 per Angstrom. The k-mesh was forced to be centered on the gamma point. The models of different structures were provided in Figure S9, Supporting Information.

The sections of characterization and photocatalytic experiments are available in the Supporting Information.

Supporting Information

Supporting Information is available from the Wiley Online Library or from the author.

Acknowledgements

This work was supported by the National Natural Science Foundation of China (Grant No.: 51978178, 51478172, 51521006, 51938007, and 51720105001), the Department of Science and Technology of Guangdong Province of China (Contract No.: 2019A1515012044 and 2018S0011), the International S&T Cooperation Program of China (Contract No.: 2015DFG92750), the Department of Science and Technology of Hunan Province of China (Contract No.: 2017JJ2029 and 2017SK2362), the National Science Foundation of Hunan Province, China (Grant No.: 2018JJ3053), the Science and Technology Innovation Program of Hunan Province, China (Contract No.: 2021RC2058), and the Shanghai Tongji Gao Tingyao Environmental Science & Technology Development Foundation.

Conflict of Interest

The authors declare no conflict of interest.

Data Availability Statement

Research data are not shared.

Keywords

charge transfer, nitrogen vacancies, photocatalysis, silver phosphate, tungsten nitrides

Received: September 1, 2021

Revised: October 21, 2021

Published online: November 10, 2021

- [1] W. L. Jiang, X. Xia, J. L. Han, Y. C. Ding, M. R. Haider, A. J. Wang, *Environ. Sci. Technol.* **2018**, *52*, 9972.
- [2] Y. Wang, Y. Yang, Y. Shi, H. Song, C. Yu, *Adv. Mater.* **2019**, *32*, 1904106.
- [3] O. Alagha, N. Ouerfelli, H. Kochkar, M. A. Almessiere, Y. Slimani, A. Manikandan, A. Baykal, A. Mostafa, M. Zubair, M. H. Barghouthi, *Nanomaterials* **2021**, *11*, 970.
- [4] R. Abazari, A. R. Mahjoub, J. Shariati, *J. Hazard. Mater.* **2019**, *366*, 439.
- [5] J. L. Wang, R. Zhuan, *Sci. Total Environ.* **2020**, *701*, 135023.
- [6] M. Dou, J. Wang, B. Gao, C. Xu, F. Yang, *Chem. Eng. J.* **2020**, *383*, 123134.
- [7] L. Xu, L. C. Campos, M. Canales, L. Ciric, *Water Res.* **2020**, *182*, 115954.
- [8] L. Chu, J. L. Wang, S. He, C. Chen, L. Wojnárovits, E. Takács, *J. Hazard. Mater.* **2021**, *415*, 125724.
- [9] D. Ş. Karaman, U. K. Ercan, E. Bakay, N. Topaloğlu, J. M. Rosenholm, *Adv. Funct. Mater.* **2020**, *30*, 1908783.
- [10] F. Sheng, J. Ling, C. Wang, X. Jin, X. Gu, H. Li, J. Zhao, Y. Wang, C. Gu, *Environ. Sci. Technol.* **2019**, *53*, 10705.
- [11] J. Zhang, Z. Xiong, J. Wei, Y. Song, Y. Ren, D. Xu, B. Lai, *Chem. Eng. J.* **2020**, *383*, 123144.
- [12] S. Lu, C. Lin, K. Lei, B. Wang, M. Xin, X. Gu, Y. Cao, X. Liu, W. Ouyang, M. He, *Water Res.* **2020**, *184*, 116187.
- [13] H. Ge, Y. Kuwahara, K. Kusu, H. Yamashita, *J. Mater. Chem. A* **2021**, *9*, 13898.
- [14] J. Yang, J. Jing, Y. F. Zhu, *Adv. Mater.* **2021**, *33*, 2101026.
- [15] H. Y. Zhu, R. Jiang, J. B. Li, Y. Q. Fu, S. T. Jiang, J. Yao, *Sep. Purif. Technol.* **2017**, *179*, 184.
- [16] A. E. Wendlandt, *Science* **2019**, *366*, 304.
- [17] Z. Jiang, X. Xu, Y. Ma, H. S. Cho, D. Ding, C. Wang, J. Wu, P. Oleynikov, M. Jia, J. Cheng, Y. Zhou, O. Terasaki, T. Peng, L. Zan, H. Deng, *Nature* **2020**, *586*, 549.
- [18] G. Murali, S. V. P. Vattikuti, Y. K. Kshetri, H. Lee, J. K. R. Modigunta, C. S. Reddy, S. Park, S. Lee, B. Poornaprakash, H. Lee, Y. H. Park, J. Lee, S. Y. Park, I. In, *Chem. Eng. J.* **2021**, *421*, 129687.
- [19] P. Dong, Y. Wang, H. Li, H. Li, X. Ma, L. Han, *J. Mater. Chem. A* **2013**, *1*, 4651.
- [20] S. Zhang, S. Zhang, L. Song, *Appl. Catal., B* **2014**, *152–153*, 129.
- [21] S. He, C. Zhai, M. Fujitsuka, S. Kim, M. Zhu, R. Yin, L. Zeng, T. Majima, *Appl. Catal., B* **2021**, *281*, 119479.
- [22] W. Su, X. Liu, L. Tan, Z. Cui, Y. Liang, Z. Li, S. Zhu, S. Wu, *ACS Sustainable Chem. Eng.* **2020**, *8*, 2577.
- [23] Y. Lin, H. Y. Liu, C. P. Yang, X. Wu, C. Du, L. M. Jiang, Y. Y. Zhong, *Appl. Catal., B* **2020**, *264*, 118479.

- [24] L. Wang, W. Chen, D. Zhang, Y. Du, R. Amal, S. Qiao, J. Wu, Z. Yin, *Chem. Soc. Rev.* **2019**, *48*, 5310.
- [25] S. Wang, H. Ge, S. Sun, J. Zhang, F. Liu, X. Wen, X. Yu, L. Wang, Y. Zhang, H. Xu, J. C. Neufeind, Z. Qin, C. Chen, C. Jin, Y. Li, D. He, Y. Zhao, *J. Am. Chem. Soc.* **2015**, *137*, 4815.
- [26] H. Jin, X. Liu, A. Vasileff, Y. Jiao, Y. Zhao, Y. Zheng, S. Z. Qiao, *ACS Nano* **2018**, *12*, 12761.
- [27] H. Yu, X. Yang, X. Xiao, M. Chen, Q. Zhang, L. Huang, J. Wu, T. Li, S. Chen, L. Song, L. Gu, B. Y. Xia, G. Feng, J. Li, J. Zhou, *Adv. Mater.* **2018**, *30*, 1805655.
- [28] M. Q. Yang, J. Wang, H. Wu, G. W. Ho, *Small* **2018**, *14*, 1703323.
- [29] D. Chen, M. Qiao, Y. R. Lu, L. Hao, D. Liu, C. L. Dong, Y. Li, S. Wang, *Angew. Chem., Int. Ed.* **2018**, *57*, 8691.
- [30] J. Li, M. Zhang, Z. Guan, Q. Li, C. He, J. Yang, *Appl. Catal., B* **2017**, *206*, 300.
- [31] H. Jin, L. Li, X. Liu, C. Tang, W. Xu, S. Chen, L. Song, Y. Zheng, S. Z. Qiao, *Adv. Mater.* **2019**, *31*, 1902709.
- [32] Z. Hu, X. Xiao, H. Jin, T. Li, M. Chen, Z. Liang, Z. Guo, J. Li, J. Wan, L. Huang, Y. Zhang, G. Feng, J. Zhou, *Nat. Commun.* **2017**, *8*, 15630.
- [33] S. Wang, X. Yu, Z. Lin, R. Zhang, D. He, J. Qin, J. Zhu, J. Han, L. Wang, H.-k. Mao, J. Zhang, Y. Zhao, *Chem. Mater.* **2012**, *24*, 3023.
- [34] Z. Xue, K. Liu, Q. Liu, Y. Li, M. Li, C.-Y. Su, N. Ogiwara, H. Kobayashi, H. Kitagawa, M. Liu, G. Li, *Nat. Commun.* **2019**, *10*, 5048.
- [35] Y. Bi, S. Ouyang, N. Umezawa, J. Cao, J. Ye, *J. Am. Chem. Soc.* **2011**, *133*, 6490.
- [36] D. J. Martin, N. Umezawa, X. Chen, J. Ye, J. Tang, *Energy Environ. Sci.* **2013**, *6*, 3380.
- [37] X. Li, X. Mao, X. Zhang, Y. Wang, Y. Wang, H. Zhang, X. Hao, C. Fan, *Sci. China Chem.* **2014**, *58*, 457.
- [38] J. Zhang, J. Chen, Y. Luo, Y. Chen, M. Kiani, X. Wei, R. Luo, G. Wang, R. Wang, *Sci. China Mater.* **2018**, *61*, 1567.
- [39] R. Tong, Y. Qu, Q. Zhu, X. Wang, Y. Lu, S. Wang, H. Pan, *ACS Appl. Energy Mater.* **2019**, *3*, 1082.
- [40] N. Wang, X. Chen, J. Jin, P. Zhang, X. Qiao, L. Cui, *Carbon* **2020**, *169*, 82.
- [41] L. Tang, C. Feng, Y. Deng, G. Zeng, J. Wang, Y. Liu, H. Feng, J. Wang, *Appl. Catal., B* **2018**, *230*, 102.
- [42] Y. Lin, S. H. Wu, C. P. Yang, M. Chen, X. Li, *Appl. Catal., B* **2019**, *245*, 71.
- [43] Y. Lin, X. Wu, Y. Han, C. P. Yang, Y. Ma, C. Du, Q. Teng, H. Y. Liu, Y. Y. Zhong, *Appl. Catal., B* **2019**, *258*, 117969.
- [44] Y. Zhou, X. Zhang, Q. Zhang, F. Dong, F. Wang, Z. Xiong, *J. Mater. Chem. A* **2014**, *2*, 16623.
- [45] Z. Sun, H. Zheng, J. Li, P. Du, *Energy Environ. Sci.* **2015**, *8*, 2668.
- [46] C. Li, Y. Du, D. Wang, S. Yin, W. Tu, Z. Chen, M. Kraft, G. Chen, R. Xu, *Adv. Funct. Mater.* **2017**, *27*, 1604328.
- [47] K. Gunaseelan, D. A. Jadhav, S. Gajalakshmi, D. Pant, *Bioresour. Technol.* **2021**, *323*, 124564.
- [48] H. Tian, M. Liu, W. Zheng, *Appl. Catal., B* **2018**, *225*, 468.
- [49] S. H. Wu, H. R. Li, X. Li, H. J. He, C. P. Yang, *Chem. Eng. J.* **2018**, *353*, 533.
- [50] P. San-Valero, H. N. Abubackar, M. C. Veiga, C. Kennes, *Bioresour. Technol.* **2020**, *300*, 122659.
- [51] J. Liu, *J. Phys. Chem. C* **2015**, *119*, 28417.
- [52] Y. Si, H. Y. Wu, H. M. Yang, W. Q. Huang, K. Yang, P. Peng, G. F. Huang, *Nanoscale Res. Lett.* **2016**, *11*, 495.
- [53] Y. Lin, S. H. Wu, X. Li, X. Wu, C. P. Yang, G. M. Zeng, Y. R. Peng, Q. Zhou, L. Lu, *Appl. Catal., B* **2018**, *227*, 557.
- [54] L. Xu, W. Q. Huang, L. L. Wang, G. F. Huang, P. Peng, *J. Phys. Chem. C* **2014**, *118*, 12972.
- [55] Y. Lin, C. P. Yang, S. H. Wu, X. Li, Y. J. Chen, W. L. Yang, *Adv. Funct. Mater.* **2020**, *30*, 2002918.
- [56] J. C. Zou, Y. Lin, S. H. Wu, Y. Y. Zhong, C. P. Yang, *Adv. Funct. Mater.* **2021**, *31*, 2100442.